



Simultaneous formation of mesopores and homojunctions in graphite carbon nitride with enhanced optical absorption, charge separation and photocatalytic hydrogen evolution



Guiming Ba^a, Zhiwei Liang^a, Haiping Li^{a,*}, Na Du^b, Jianqiang Liu^c, Wanguo Hou^b

^a National Engineering Research Center for Colloidal Materials, Shandong University, Jinan 250100, PR China

^b Key Laboratory for Colloid and Interface Chemistry (Ministry of Education), Shandong University, Jinan 250100, PR China

^c School of Microelectronics, Shandong University, Jinan 250100, PR China

ARTICLE INFO

Keywords:

Graphite carbon nitride
Homojunction
Cyanuric
Hydrogen evolution
Photocatalytic

ABSTRACT

Graphite carbon nitride (CN) is considered as a promising photocatalyst for solving current energy and environmental crises, but its practical application is still restricted by fast recombination of photogenerated charge carriers, low specific surface area, and narrow visible light absorption range. Herein, oxygen-modified CN (MCN) with simultaneous formation of massive mesopores and homojunctions was successfully synthesized by calcining the precursor, a cyanuric acid (CYA)-loaded melamine (MA) hierarchical structure composed of nanobelts, which was prepared for the first time. MCN exhibits accelerated charge separation, increased specific surface areas, and enhanced visible light absorption, compared with CN, and these jointly render the photocatalytic hydrogen evolution rate of MCN ($934 \mu\text{mol h}^{-1} \text{g}^{-1}$) be about five times higher than that of CN ($163 \mu\text{mol h}^{-1} \text{g}^{-1}$). MCN also exhibits much faster singlet oxygen generation and higher photoactivity in organic degradation. The MA hierarchical structure and CYA synergistically formed the new mesopores and C–O–C bonds in MCN, which cause prominent upper shift of the Fermi level and enhanced photoabsorption of MCN. Besides, electronic microscopy images distinctly show two different sorts of regions in MCN, i.e. those with massive and few mesopores (marked as MPCN and NPCN), respectively. Therefore, MPCN/NPCN homojunctions were probably constructed in MCN, which leads to the accelerated charge separation. This work gives a way to form simultaneously mesopores and homojunctions in CN and illustrates the formation mechanism, which can effectively direct synthesis of similar photocatalysts.

1. Introduction

Graphite carbon nitride (CN) is one of the most attractive visible-light-responsive photocatalysts in recent years because of its wide availability, non-toxicity, high chemical stability and versatile application for solar energy conversion, such as photocatalytic hydrogen evolution, carbon dioxide reduction, nitrogen fixation, selective transformation of organics, and contaminant degradation. However, fast photogenerated charge recombination, low specific surface area and a narrow photoabsorption spectrum range of CN seriously restrict its practical application [1–4].

To overcome above-mentioned defects of CN, many ways have been proposed and given rise to positive outcomes for photoactivity enhancement, such as morphological manipulation, structural modification, elemental doping, exfoliation, and construction of homo- or hetero-junction [5–13]. Generally, there are several ways working

simultaneously. For instance, the elemental doping can be accompanied with morphological change; [14] the structural modification usually included the elemental doping; [15] and the construction of junction, especially homojunction, inevitably referred to the morphological variation [8]. Therefore, one strategy generally causes changes of several factors all of which benefit photoactivity improvement. For example, Zhang and coauthors prepared vine-like CN with significantly enhanced charge separation efficiency and photoabsorption, as well as increased specific surface area; [5] Rahman et al. synthesized amorphous CN with high specific surface area, strengthened photoabsorption, and slowing charge recombination; [16] and Qiu et al. prepared highly crystalline K-intercalated CN exhibiting enhanced optical absorption and accelerated charge separation [17]. Overall, association of two or more ways to improve photoactivity of CN is a satisfactory choice.

Homojunction fabrication is the most efficient way to increase the

* Corresponding author.

E-mail address: hpli@sdu.edu.cn (H. Li).

charge separation efficiency without introduction of other elements. Theoretically, construction of CN homojunction is an easy-to-realized strategy in consideration of that CN, synthesized by using different raw materials (e.g. melamine (MA), urea, thiourea, cyanamide, dicyandiamide, and their mixtures) and different calcination ways (e.g. in air and in inert gas) [18], possesses different energy band levels. The energy band level difference may arise from difference in crystallinity, defect types and amount, and bonding ways and amount of residual oxygen in synthetic processes. For example, Wang and coauthors synthesized semicrystalline CN with homojunction fabricated between orderly and disorderly areas, exhibiting excellent performance in charge separation; [8] Liu et al. successfully prepared CN p-n homojunctions via introduction of defects and C≡N groups and these homojunctions exhibit substantially accelerated charge separation and increased optical absorption; [19] and Tan et al. prepared mesoporous CN/CN nanosheet homojunctions with a high specific surface area and an increased charge separation efficiency [20]. Besides, CN metal-free homojunction [21], exfoliated CN homojunction [22], and amorphous/crystalline CN homojunction [23] were also reported. Overall, based on current cost-effective and facile CN homojunction fabrication techniques, more homojunctions should be synthesized from the perspective of both theory and application. In addition, increasing the specific surface area by introduction of mesopores via morphological manipulation can considerably improve the photocatalytic performance because of more exposed active sites and probable enhanced photoabsorption [24,25], but simultaneous formation of mesopores and homojunctions were rarely reported before and related mechanism for the homojunction fabrication need be expounded.

In this work, CN homojunctions with massive mesopores were simply synthesized via polycondensation of cyanuric acid (CYA)-loaded melamine (MA) hierarchical structure. The homojunctions, constructed between regions with massive mesopores and those with few mesopores, exhibit considerably accelerated charge separation beside increased specific surface area and photoabsorption, and thus improved photocatalytic activity in hydrogen evolution and organic degradation. This work illustrates the mechanism for CN homojunction fabrication, which can direct construction of a subsequent series of homojunctions.

2. Experimental

2.1. Materials

MA (99%), trichloroisocyanuric acid (TCCA, 99%), CYA (98%), ethanol (99.5%), ethylene glycol (99.5%), rhodamine B (RhB, 99.0%), and triethanolamine (TEOA, 99.5%) were bought from Aladdin (China). NaClO (Cl content of ≥ 10 wt%, AR) and concentrated HCl (36.0–38.0 wt%, AR) solutions were purchased from Damao Chemical Reagent Factory (China) and Sinapharm (China), respectively. The 5,5'-dimethyl-1-pyrroline-N-oxide (DMPO, 97%) and the 2,2,6,6-tetramethylpiperidine (TEMP, 99%) were purchased from Sigma. All the chemicals were used as received.

2.2. Preparation of precursors

Typically, x g of TCCA was dissolved in 80 mL of ethanol, after which $(10 - x)$ g of MA was added and dispersed in the solution. Then, the dispersion was heated at 70 °C under magnetic stirring until completely dried. The resultant white powder continued to be dried at 60 °C for 12 h in an oven, and the final product was marked as MA/TCCA- x . Herein, x equals to 1, 2, 3 or 4.

For comparison, the precursor MA/CYA was prepared via a similar procedure as MA/TCCA-2 except that 1.1 g of CYA was substituted for 2 g of TCCA. The precursor MA/CYA-W was prepared through a similar process as MA/CYA except the ethanol was replaced by water. The precursor MA/HClO was also similarly prepared. Simply, 8 g of MA was dispersed in 80 mL of ethanol. Then, 9 g of NaClO solution and 2 mL of

concentrated HCl solution were added to the dispersion and heated at 70 °C under magnetic stirring until completely dried. The resultant white powder continued to be dried at 60 °C for 12 h in an oven. The samples MA/ethanol and TCCA/ethanol were also prepared by a similar way as MA/TCCA-2 except TCCA and MA were not added, respectively.

2.3. Preparation of CN homojunctions

Ten grams of MA/TCCA- x were transferred into a lidded crucible which was then placed in a muffle furnace and heated at 550 °C for 4 h in air with a ramp rate of 5 °C min⁻¹. After naturally cooled to the room temperature, the sample was ground into powder which was subsequently dispersed in 200 mL of water and stirred for 12 h. After filtration, washing with water and drying at 60 °C for 24 h, the final product was obtained and denoted as MCN- x . Pure CN was prepared via a similar way as MCN- x except replacing MA/TCCA- x by MA. The precursors MA/CYA, MA/CYA-W, and MA/HClO were also calcined and processed via a similar procedure as MA/TCCA- x , and the final products were marked as MCN-CYA, MCN-CYA-W and MCN-HClO, respectively.

2.4. Characterizations

Powder X-ray diffraction (XRD) was performed on a PAN analytical X'Pert³ diffractometer with Cu K α radiation ($\lambda = 1.54056$ Å) and a scanning rate of 5°/min. X-ray photoelectron spectroscopy (XPS) was carried out on a Thermo Scientific Escalab 250Xi spectrometer with Al K α radiation ($h\nu = 1486.6$ eV). All peak positions were calibrated by the C 1s peak at 284.6 eV A Zeiss Supra55 field emission-scanning electron microscope (SEM) equipped with an energy dispersive X-ray spectrometer (EDS) and a Jeol JEM-1011 transmission electron microscope (TEM) were used for morphological observation. UV-vis diffuse reflectance spectroscopy was carried out on a Hitachi U-4100 spectrophotometer. Fourier transform infrared (FT-IR) spectra were measured on a Bruker Tensor 27 spectrophotometer. Photoluminescence (PL) spectroscopy was performed on a Hitachi F-7000 spectrophotometer with an excitation wavelength of 380–420 nm and excitation and emission slit widths of 5.0 and 2.5 nm, respectively. Time-resolved fluorescence decay spectroscopy was performed on an FLS980 time-resolved spectrofluorometer (Edinburgh Analytical Instruments) with excitation and monitoring wavelengths of 400 and 463 nm, respectively. N₂ sorption isotherms were tested on a Quantachrome NOVA2000E instrument at liquid nitrogen temperature. All the samples were degassed at 120 °C for 4 h before tests. Electron paramagnetic resonance (EPR) spectroscopy was performed on a Bruker A300-1012 spectrometer at the room temperature. To detect hydroxyl radicals (·OH), superoxide radicals (·O₂[−]), and singlet oxygen (¹O₂), DMPO (100 mM), DMPO in methanol, and TEMP (100 mM) were used as in situ trapping agents, respectively. Aqueous suspensions (5 mg/mL) of the samples and the appropriate spin trap were drawn by a capillary tube and inserted into a narrow quartz tube. The tube was then placed in the EPR cavity and the spectra were recorded before and after illumination through the EPR cavity, by using a 300-W Xe lamp (CEL-XHF300, Ceaulight, China) with a cutoff filter ($\lambda \geq 420$ nm, Ceaulight). The EPR measurement conditions were listed as follows: Frequency, 9.85 GHz; Microwave power, 19.15 mW; Scan width, 100 G; Resolution, 1024; Receiver gain, 1×10^3 ; Conversion time, 30 ms; Time constant, 20 ms; Sweep time, 30.72 s; Scans, 2; and Modulation frequency, 100 kHz.

2.5. Photoelectrochemical tests

All of photoelectrochemical measurements were carried out on a CHI660E electrochemical workstation (Chenhua, China) with a standard three-electrode system soaked in a 0.2 M Na₂SO₄ solution. Ag/AgCl and Pt wire were used as reference and counter electrodes, respectively. Potentials measured against the Ag/AgCl electrode were

corrected to the NHE via the equation $E(\text{NHE}) = E(\text{Ag}/\text{AgCl}) + 0.21 \text{ V}$. Working electrodes were prepared by coating sample slurries onto clean ITO glass, followed by dried at 60 °C for 24 h and calcined at 100 °C for 2 h in N₂ atmosphere. The slurries were obtained by grinding mixtures of 0.02 g of samples and 100 μL of ethylene glycol. For photocurrent density tests, the applied bias is 0.6 V A 300-W xenon lamp (CEL-XHF300, Ceaulight) with a cutoff filter ($\lambda \geq 420 \text{ nm}$, CEL-UVIRCUT420, Ceaulight) were used as the light source. For Mott-Schottky tests, selected frequencies are 0.8, 0.9 and 1.0 kHz.

2.6. Photocatalytic tests

For photocatalytic hydrogen evolution (PHE), 20 mg of photocatalyst was dispersed in 80 mL of aqueous solution containing 10 vol% of TEOA. About 1.59 mL of 1.0 g L⁻¹ H₂PtCl₆ solution (with a Pt/photocatalyst weight ratio of 3 wt%) may be added to the suspension. After sonication for 10 min, the solution was transferred to a reaction cell, and vacuumed under stirring. For Pt photodeposition, a 300-W Xe lamp (CEL-XHF300, Ceaulight) was used as the light source and the irradiation time is 2 h. Then, the reaction cell was vacuumed again and the 300-W Xe lamp with a cutoff filter ($\lambda \geq 420 \text{ nm}$, CEL-UVIRCUT420, Ceaulight) was used as the visible light source for the PHE reaction. The amount of generated hydrogen was monitored by gas chromatography (TCD, GC-7920, Ceaulight) every one hour with ultrapure N₂ as the carrier gas. For measurement of the apparent quantum yield (AQY), the aforementioned CEL-UVIRCUT420 cutoff filter was replaced with a THORLABs FB420-10 band-pass filter ($\lambda = 420 \pm 2 \text{ nm}$). Average irradiation intensity (E) and the irradiation area (A) of the light are 3.9 mW cm⁻² and 3.48 cm², respectively. Then, AQY was calculated through the equation, $\text{AQY} = (2hcN_A r_H)/(EA\lambda) \times 100\%$ where h , c , N_A , and r_H , are the Planck constant ($6.626 \times 10^{-34} \text{ J s}$), the light rate ($3.0 \times 10^8 \text{ m s}^{-1}$), the Avogadro's constant ($6.02 \times 10^{23} \text{ mol}^{-1}$), and the H₂ evolution rate (mol s⁻¹), respectively.

Photodegradation reactions were performed on a XPA-7 photocatalytic reaction apparatus (Xuijiang Electromechanical Plant, China) [26]. A 500-W xenon lamp with a cutoff filter ($\lambda \geq 420 \text{ nm}$) was used as the light source. For each run, 0.02 g of the sample was added to 50 mL of 10 mg L⁻¹ RhB solution. The suspension was then stirred in the dark for 1 h to reach sorption equilibrium. After light is on, about 4 mL of the suspension was taken out every constant interval and filtered through 0.45-μm poly(ether sulfone) syringe filters. Absorbance of filtrates was analyzed on a Hewlett-Packard 8453 UV-vis spectrophotometer.

3. Results and discussion

3.1. Synthesis and morphologies of CN homojunctions

Simple synthetic routes for various precursors and photocatalysts were schematically shown in Fig. 1. The commercial MA is composed of irregular blocks with sizes from several to several tens of micrometers (Figs. 1a and 2 a). When dispersed in the TCCA methanol solution and heated, TCCA can completely react with residual water in the ethanol and vapor from air to generate CYA and HClO [27] (Fig. S1, Supporting Information), as evidenced by FT-IR spectra of samples (Fig. S2 and Table S1, Supporting Information). Interestingly, in this process, MA blocks all become hierarchical structure composed of nano-belts or -rods, and irregular CYA particles with sizes of several to hundreds of nanometers adhere to surfaces of MA (Figs. 1b, 2 b, 2 c and S3, Supporting Information). The EDS spectrum of MA/TCCA-2 shows existence of C, N, O, and Cl elements, suggesting residue of HClO (Fig. 2d), and its elemental mapping images display homogeneous distribution of CYA and residual HClO on MA surfaces (Inset in Fig. 2d). The high structural stability of MA in the synthetic process of MA/TCCA-2 can be confirmed by FT-IR spectra and XRD patterns (Figs. S4 and S5, Supporting information). The close contact of MA with CYA and HClO probably arises from hydrogen bonding interactions between

them [28] (see analyses on FT-IR spectra of samples in Fig. S4).

To clarify the mechanism for formation of MA hierarchical structure, probable influencing factors were investigated, such as solvent (ethanol), TCCA, HClO, and CYA. Results show that the solvent and CYA hardly induce change of MA blocks though CYA particles can also distribute on surfaces of MA, as shown by SEM images of MA/ethanol and MA/CYA (Fig. S6a-d, Supporting Information). TCCA itself can only be hydrolyzed into CYA octahedral blocks with sizes of several micrometers (Fig. S6e and f). HClO can indeed cause MA blocks to become hierarchical structure composed of belt-like particles, as shown by SEM images of MA/HClO (Fig. S6h and i), suggesting its decisive role for formation of MA hierarchical structure in MA/TCCA-x. The hierarchical structure is formed probably via an “incision or etching” process of HClO. HClO can form hydrogen bonding complex with MA (Fig. S1), which may be slightly dissolved in the solvent. The dissolution and recrystallization process of MA ultimately leads to formation of the hierarchical structure. Difference between MA hierarchical structure in MA/TCCA-2 (Fig. 2c) and that in MA/HClO (Fig. S6i) indicates that CYA also affects formation of the hierarchical structure in MA/TCCA-x, probably by strong hydrogen bonds between CYA and MA. With increasing x , nano-belts or -rods in the hierarchical structure of MA/TCCA-x become shorter and thicker (Figs. 2c and S3(c, f, and i)), suggesting the significant influence of HClO concentrations. According to our best knowledge, synthesis of MA hierarchical structure via a so simple route is reported for the first time.

When calcining MA/TCCA-2, MA around the CYA may polycondense into CN with massive new mesopores (MPCN) and that far from the CYA into CN with few mesopores (NPCN, Fig. 1c), as shown by arrows and circles in SEM and TEM images (Figs. 2e-h, and S7), respectively. Similar results were obtained for MCN-4 (Fig. S8, Supporting Information). The morphology of NPCN is just like pure CN (Fig. S9, Supporting Information). There are three possible reasons for formation of the new mesopores. The first one is the hierarchical structure of the precursor. The second one is that small CYA particles on MA nanobelts work as the blocker for MA polymerization because of the gradual removal of CYA upon heating, which can be verified by the fact that when calcining pure CYA at 550 °C for 4 h, nothing was left. The third one is decomposition of CYA may generate water which can etch CN framework at high temperature [7]. The EDS spectrum of MCN-2 shows existence of C, N, and O (Fig. 2i) and corresponding elemental mapping images show their homogeneous distribution in the sample (Inset in Fig. 2i). The element Cl was undetectable, indicating its complete removal in the calcination process.

3.2. Structure and properties

To further confirm formation of above-mentioned new mesopores, N₂ absorption-desorption isotherms of CN and MCN-x were tested. As shown in Fig. 3a, all the samples show a type-IV isotherm featured with a type-H3 hysteresis loop, indicating existence of slit-like mesopores originating from stacking of CN nanosheets [29]. BET specific surface areas (S_{BET}) of MCN-x (8.8–14.6 m² g⁻¹) are higher than that of CN (6.7 m² g⁻¹) and the S_{BET} of MCN-x increases then decreases with increasing x . MCN-2 possesses the highest S_{BET} (Fig. 3a). Pore size distribution curves of samples are shown in Fig. 3b. CN possesses only a few mesopores with pore sizes of ~6–100 nm, while MCN-x generates new mesopores with pore sizes of ~2–6 nm, beside increase in amount of mesopores of ~6–100 nm, which accords quite well with the SEM and TEM results. Pore volume of samples also increases initially and decreases then from CN to MCN-3 with MCN-2 possessing the greatest pore volume (0.062 cm³ g⁻¹).

MCN-HClO, MCN-CYA, and MCN-CYA-W all show similar N₂ sorption isotherms (Fig. S10a, Supporting Information) and pore size distribution curves (Fig. S10b) as MCN-2, but their S_{BET} (8.9, 11.3, and 11.1 m² g⁻¹, respectively) and pore volume (0.030, 0.032, and 0.021 cm³ g⁻¹, respectively) are smaller than those of MCN-2,

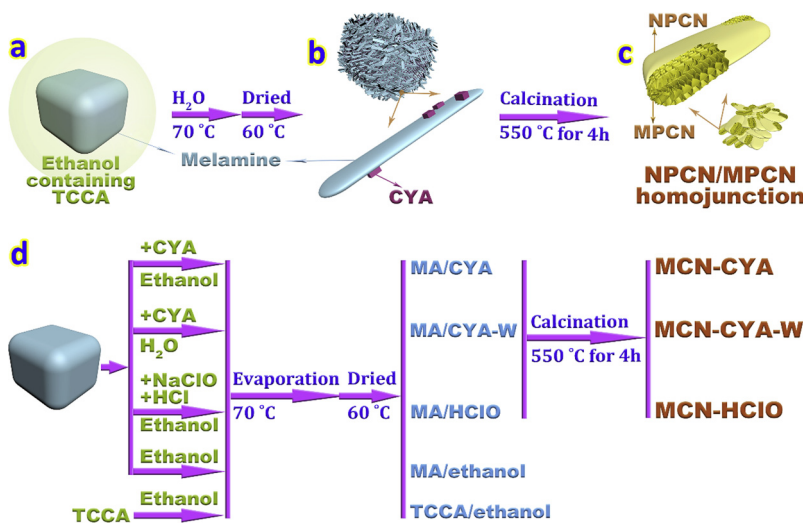


Fig. 1. (a–c) Schematic illustration for the synthetic route of CN homojunction and structures of (b) the precursor MA/TCCA-x and (c) the MPCN/NPCN homojunction; and (d) simple route diagrams for preparation of various precursors and corresponding photocatalysts. MPCN and NPCN in (c) denote regions with massive and few mesopores, respectively.

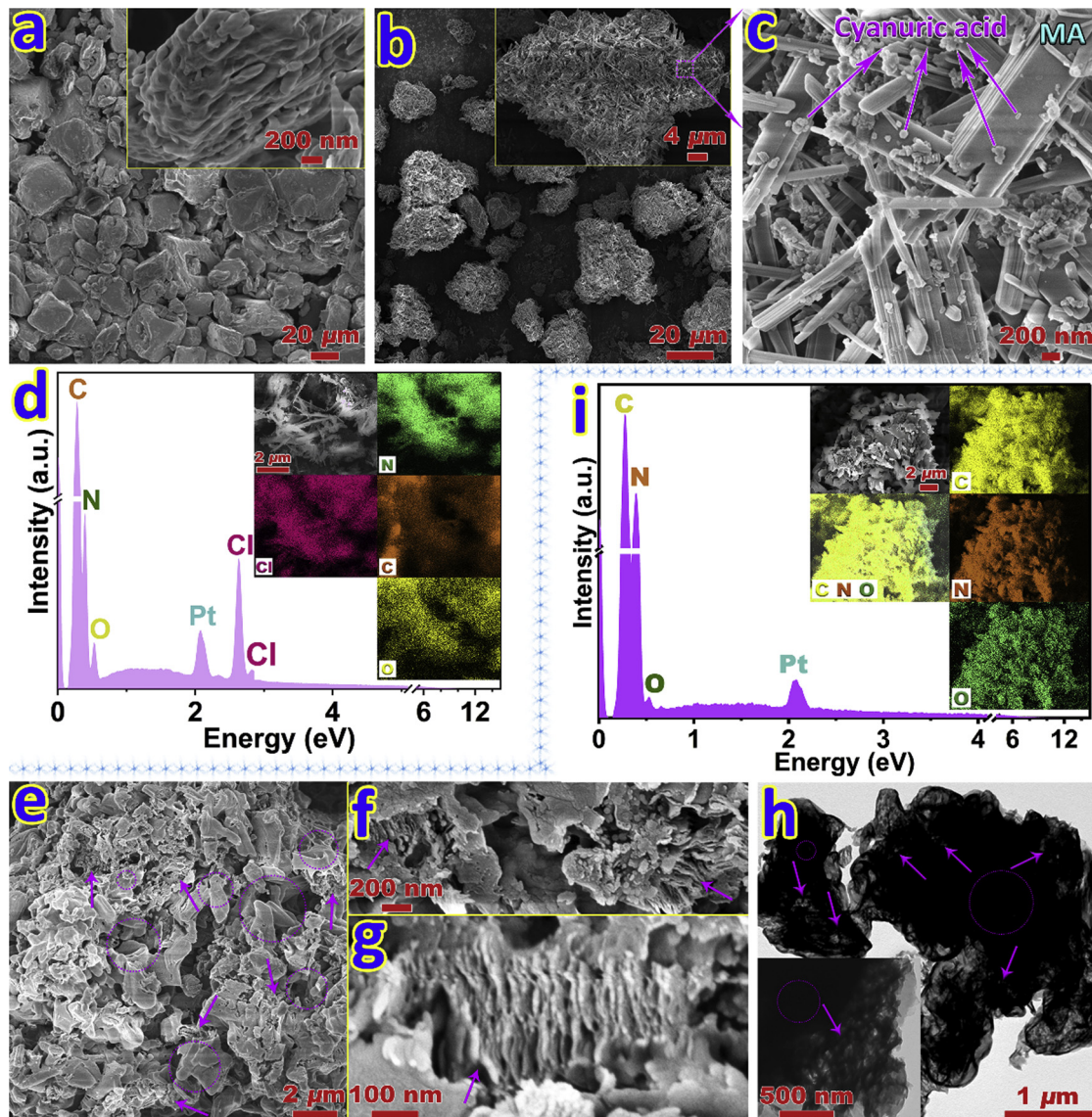


Fig. 2. SEM images of (a) MA, (b and c) MA/TCCA-2, and (e–g) MCN-2; (h) TEM images of MCN-2; and EDS spectra and elemental mapping images of (d) MA/TCCA-2 and (i) MCN-2. Arrows in (e–h) point at new mesoporous regions. Dotted circles in (e and h) denote regions with few mesopores.

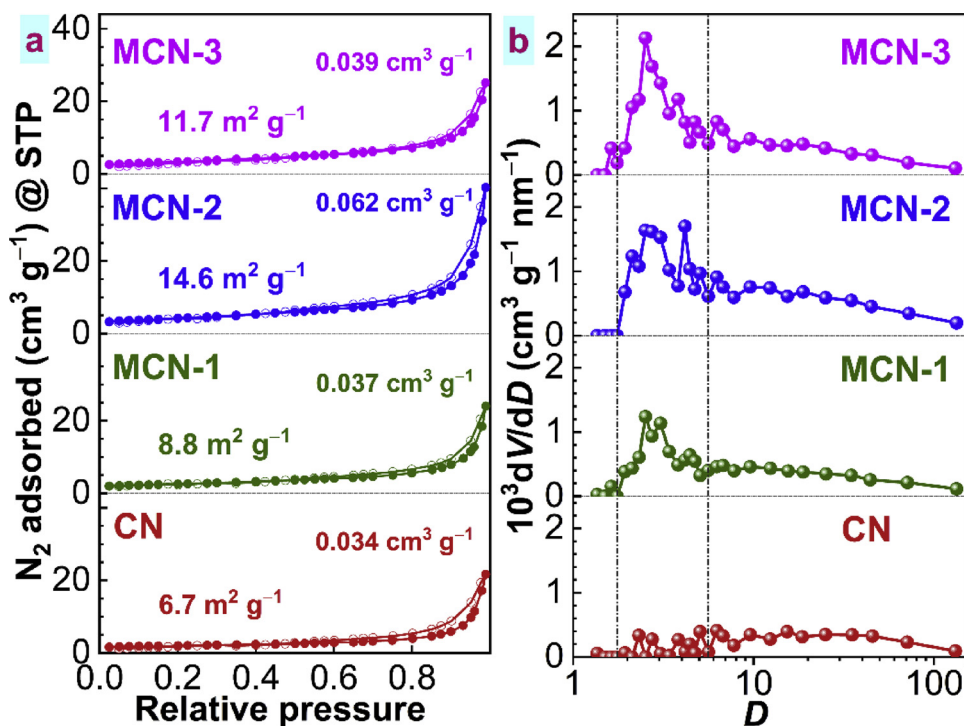


Fig. 3. (a) N₂ sorption isotherms and (b) pore size (D) distribution curves calculated from adsorption branches of isotherms by a BJH method for different samples. Numbers in (a) are BET specific surface areas (m² g⁻¹) and pore volume (cm³ g⁻¹).

suggesting synergism of the MA hierarchical structure and CYA for formation of MCN-2 with new mesopores and high S_{BET} and pore volume.

Fig. 4a shows XRD patterns of samples. Diffraction peaks of CN at 13.0 and 27.5° are attributed to in-plane repeated units and interlayer stacking reflection, respectively [30]. These two peaks for MCN-x become weak, indicating decreased crystallinity. Generation of mesoporous structure usually leads to decrease in the crystallinity [24,31]. Overall, no impurity peaks are observed for MCN-x, indicating they possess similar framework structure as CN. XRD patterns of MCN-HClO, MCN-CYA, and MCN-CYA-W also show similar but weaker diffraction peaks as/than that of CN (Fig. S10c).

Fig. 4b shows FT-IR spectra of samples. All the samples show similar absorption bands at ~3425, 890–1800 and 808 cm⁻¹, which are assigned to surficial O–H stretching vibration [32,33], C=N and C–N stretching vibration [26,34] and the characteristic breathing mode of *s*-triazine [26,35], respectively. Absorption peaks at 3335–2885 cm⁻¹ are ascribed to N–H stretching vibration [32,33]. MCN-x exhibits a blueshift of the adsorption peaks, compared with CN. Blueshift distance of the peaks increases then decreases with increasing x , and MCN-2 exhibits the most prominent blueshift, as shown by solid lines and arrows in the figure. Besides, peak intensity ratios of O–H to N–H for the samples also initially increases and then decreases with increasing x , and MCN-2 possesses the greatest ratio (Fig. 4b). The blueshift of N–H peaks probably stems from hydrogen bonds between N–H and O-containing groups.

XPS spectra were measured to further determine structure of samples. XPS survey spectra show existence of only C, N, and O in CN and MCN-x (Fig. S11a, Supporting Information). Cl 2p core-level spectra of MCN-x show no peaks (Fig. S11b), indicating negligible Cl residue. Fig. 4c shows C 1s, N 1s, and O 1s core-level spectra of the samples. In the C 1s spectra, peaks at the binding energy (BE) of 284.6 eV for all the samples are assigned to adventitious C [36]. For CN, peaks at BEs of 287.99 and 288.79 eV are assigned to C in N=C–N and surficial C–OH bonds, respectively [37]. MCN-x shows similar N=C–N peak positions as CN, but shift of C–OH peaks to lower BE positions than CN. MCN-2

displays the most prominent shift, ~0.14 eV N 1s core-level spectra of the samples show similar peaks and peak positions. Peaks at BEs of 398.49, 399.73, and 401.03 eV are assigned to N in C=N=C, N–C₃, and N–H bonds, respectively [38]. The O 1s core-level spectrum of CN shows one peak at 532.02 eV which corresponds to O in surficial C–OH bonds and adsorbed H₂O [2]. O 1s peaks of MCN-x shift to higher BE positions compared with that of CN, and MCN-2 shows the most prominent shift, ~0.24 eV. The shift of C–OH peaks of MCN-x (especially MCN-2) in the C 1s and O 1s spectra possibly results from formation of C–O–C bonds in the presence of CYA, where O stays in the linker position [6] (Fig. S12a, Supporting Information). The most prominent shift for MCN-2 suggests MCN-2 contains the most C–O–C bonds. To evidence existence of C–O–C bonds in MCN-x, O 1s core-level spectra of Ar⁺ etched CN and MCN-2 were also tested. As shown in the O 1s spectra, the peak of CN becomes quite weak because of removal of most surficial hydroxyl species, and peak intensity of MCN-2 is much higher than that of CN, suggesting existence of C–O–C bonds in the bulk rather than on the surface of MCN-2.

According to the XPS data and elemental analysis results, N/C molar ratios of pure CN and MCN-x are similar (Tables 1 and S2, Supporting Information), suggesting their similar basic framework structure of molecules. However, molar ratios of C atoms in C–O bonds (including C–O–C and C–OH) to those in N=C–N bonds increase then decrease from CN to MCN-3 with MCN-2 exhibiting the greatest value, suggesting more C–O bonds, especially C–O–C bonds formed in MCN-2 than in CN. From CN to MCN-3, molar ratios of N–C₃/N decrease then increase and those of C–O/N–H increase then decrease, with MCN-2 possessing the smallest and the greatest values, respectively, while N–H/N molar ratios almost keep changeless (Table 1). This suggests the increase of C–O bond content is accompanied with the reduction of N–C₃ bonds in MCN, which may eventually lead to decrease of the nanosheet size and benefits increase of the S_{BET} (Fig. S12b). Besides, MCN-2 possesses the greatest intensity ratio of O–H to N–H peaks in the FT-IR spectra (Fig. 4b), also suggesting the most C–OH bonds in MCN-2.

Photoabsorption performance of samples were investigated via

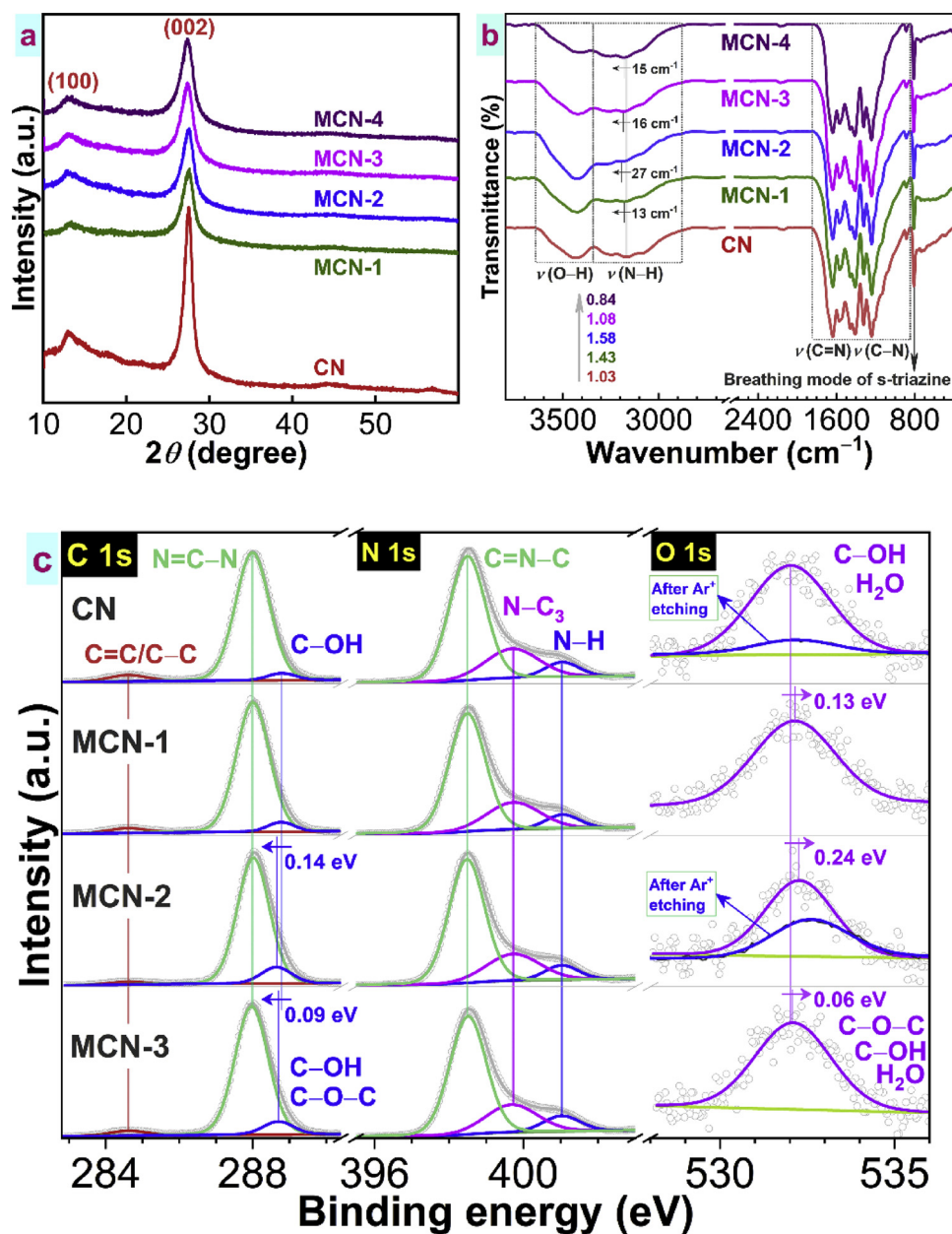


Fig. 4. (a) XRD patterns, (b) FT-IR spectra, and (c) XPS C 1s, N 1s and O 1s core-level spectra of different samples.

Table 1
Elemental molar ratios calculated from XPS data of different samples.

Sample	N/C molar ratio	C—O/N—C=N ^a	N—C ₃ /N ^b	N—H/N ^c	C—O/N—H ^d
CN	1.29	0.048	0.239	0.078	0.44
MCN-1	1.29	0.062	0.234	0.075	0.59
MCN-2	1.29	0.125	0.225	0.077	1.09
MCN-3	1.28	0.095	0.228	0.092	0.72

^a Molar ratio of C in C—O bonds to C in N—C=N bonds.

^b Molar ratio of N in N—C₃ bonds to all the N atoms.

^c Molar ratio of N in N—H bonds to all the N atoms.

^d Molar ratio of C in C—O bonds to N in N—H bonds.

UV-vis diffuse reflectance spectroscopy. As shown in Fig. 5a, visible light absorption of MCN-x is higher than that of CN, which is consistent with darkening color of samples (Inset in Fig. 5a). The extended absorption tails of MCN-x in the visible light region should arise from the oxygen introduction (see above discussion on XPS results) [6]. Tauc

plots of samples were gained via the equation, $a\hbar\nu = A(\hbar\nu - E_g)^n/2$ where a , A , \hbar and ν are the absorption coefficient, the constant, the Planck constant and the light frequency, respectively. The parameter n represents transition characteristics of semiconductors ($n = 1$ for direct bandgap transition and $n = 4$ for indirect bandgap transition) [39]. CN is generally a direct bandgap semiconductor, i.e. n equals to 1 [34]. Then, bandgaps of CN, MCN-1, MCN-2, and MCN-3 are determined to be ~2.78, 2.77, 2.77, and 2.76 eV, respectively (Inset in Fig. 5a). Overall, their bandgaps are similar.

EPR spectra of samples were tested to analyze unpaired electrons (Fig. 5b). One single Lorentzian line centered at g of 2.0044 was detected for CN. This g value is ascribed to unpaired electrons of π -bonded aromatic rings [39]. For MCN-2, the g value decreases to 2.0039 and the EPR signal in the dark strengthens, revealing increased unpaired electron density or electronic delocalization [39,40], which probably results from the introduction of O atoms [41] (Fig. S12a). This benefits charge transfer [42]. Besides, EPR signals of both MCN-2 and CN under light irradiation are stronger than those in the dark, indicating an

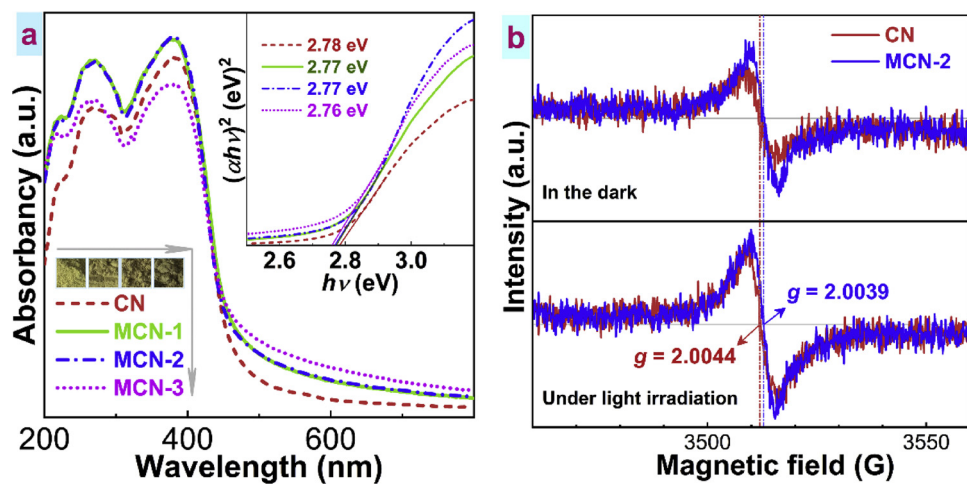


Fig. 5. (a) UV-vis diffuse reflectance spectra, (Inset in a) corresponding Tauc plots, and (b) EPR spectra of samples. Pictures of samples and energy bandgaps of samples are also shown in (a).

increase in unpaired electron concentrations because of photogenerated charge separation.

3.3. Photogenerated charge separation

Photogenerated charge separation is the premise of photocatalysis [18]. PL spectra of samples are shown in Figs. 6a and S13 (Supporting Information). PL intensity of MCN-x is lower than that of CN and becomes lower and lower with increasing x , indicating slowing photogenerated charge recombination [29]. Time-resolved fluorescence spectra of CN and MCN-2 were tested to determine their fluorescence lifetimes. As shown in Fig. 6b, the decay curves can be well fitted to a bi-exponential model, $I(t) = B_1 \exp(-t/\tau_1) + B_2 \exp(-t/\tau_2)$ where I is the intensity, τ_1 and τ_2 are separately the short and the long fluorescence lifetimes, and B_1 and B_2 are the amplitudes of corresponding components. Both τ_1 and τ_2 of MCN-2 are longer than those of CN, but relative intensity of τ_1 and τ_2 (Int_1 and Int_2) are quite different between CN and MCN-2 (Numbers in Fig. 6b). Therefore, their mean lifetimes (τ_m) were calculated via the equation, $\tau_m = (Int_1 \cdot \tau_1^2 + Int_2 \cdot \tau_2^2) / (Int_1 \cdot \tau_1 + Int_2 \cdot \tau_2)$. The τ_m of MCN-2 (0.932 ns) is also longer than that of CN (0.754 ns), suggesting the decreased charge recombination efficiency. Photogenerated electrons with long lifetime can boost surface reactions and thus enhance photoreactivity [43]. Photocurrent density can more directly reflect the charge separation efficiency. As shown in Fig. 6c, photocurrent density of samples increases then decreases from CN to MCN-3 with MCN-2 exhibiting the highest value, indicating the much faster charge separation for MCN-2 than for CN.

3.4. Energy band levels

To elucidate the mechanism for accelerated charge separation, energy band levels of samples are studied roughly. Fig. 7a shows Mott-Schottky curves of samples. Flat band potentials of CN, MCN-1, MCN-2, and MCN-3 are determined to be -0.66, -0.63, -0.61, and -0.64 V (vs NHE), respectively, as shown by the straight extension lines. Positive slopes of the lines manifest that all the samples are n-type semiconductors [44]. Then, their conduct band (CB) minimum (E_{CBM}) can be considered proximately equal to their flat band potentials [45]. In association with the bandgaps (E_g) of samples, their valence band (VB) maximum (E_{VBM}) can be figured out via the equation, $E_{VBM} = E_g + E_{CBM}$. VB-XPS spectra of samples were tested to confirm energy (potential) difference (E_D) between E_{VBM} and Fermi levels (E_F). As shown in Fig. 7b, E_D values of CN, MCN-1, MCN-2, and MCN-3 are 2.06, 2.22, 2.34, and 2.06 eV (V), respectively. Then, E_F (vs NHE) can be confirmed via the equation, $E_F = E_{VBM} - E_D$. Energy band levels of samples are shown in Fig. 7c. On the whole, E_{CBM} and E_{VBM} of samples are similar, but E_F prominently gets higher first and lower then from CN to MCN-3 with MCN-2 possessing the highest E_F , suggesting the formation of MPCN or the oxygen introduction induces change of electronic structure of MCN-x.

The distinct E_F difference between CN and MCN-2 indicates remarkable E_F difference between NPCN and MPCN because energy band levels of NPCN can be roughly considered to be the same as those of CN. Since energy band levels of MPCN cannot be directly gained, some inference is necessary to determine their rough positions relative to

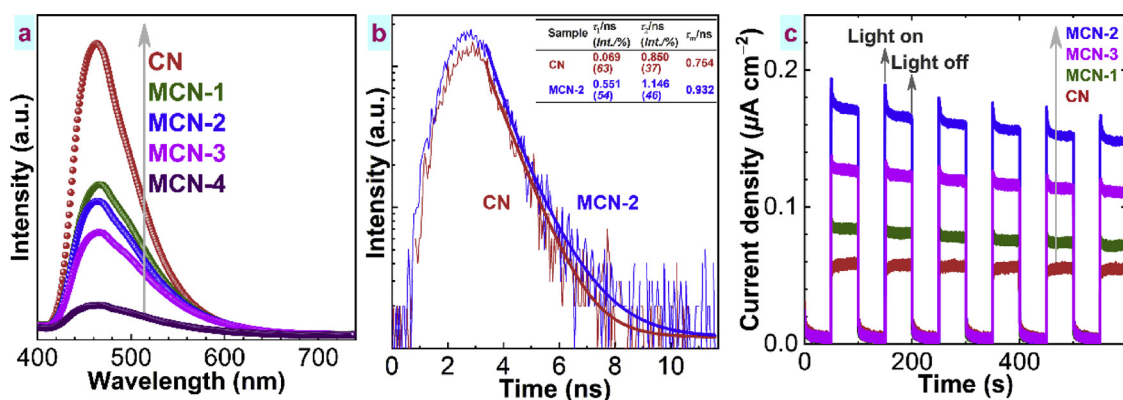


Fig. 6. (a) PL spectra, (b) time-resolve fluorescence spectra, and (c) current density of samples. Current density of samples in the dark in (c) was set at zero for distinct comparison of photocurrent density.

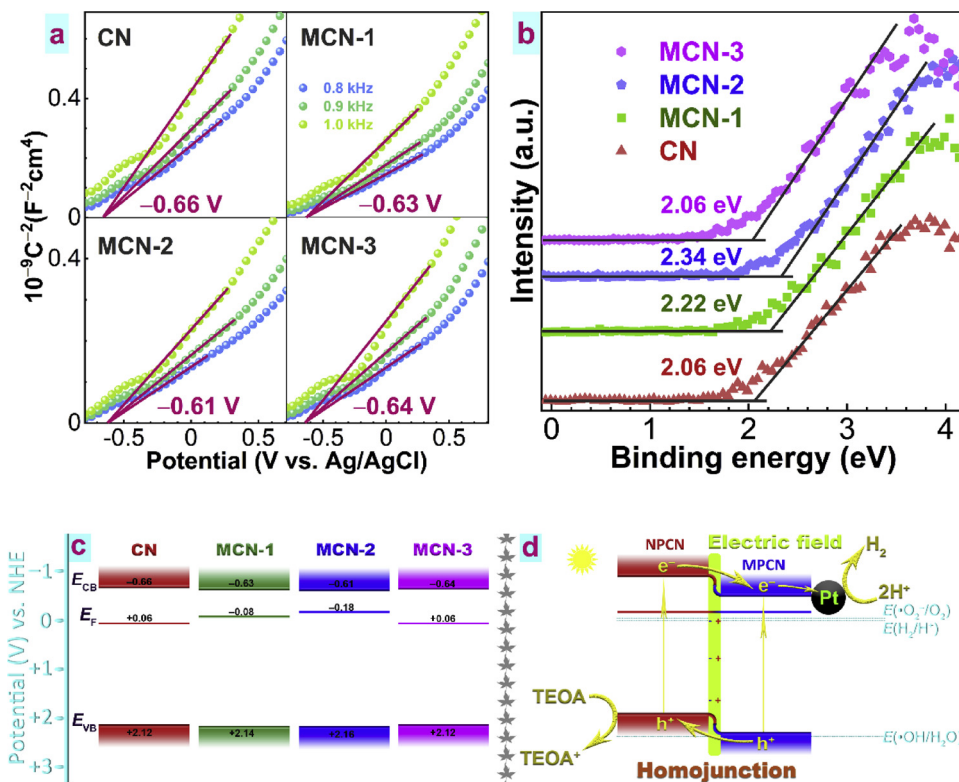


Fig. 7. (a) Mott-Schottky plots, (b) valance-band XPS spectra, and (c) energy band levels of different samples; and (d) probable charge transfer in CN homojunction.

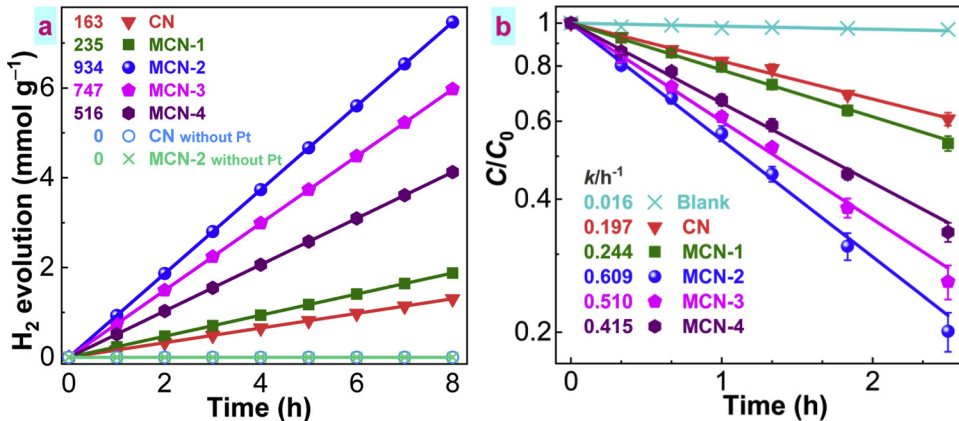


Fig. 8. (a) Photocatalytic hydrogen evolution and (b) RhB photodegradation on different samples. Numbers in (a) and (b) are hydrogen evolution rates ($\mu\text{mol g}^{-1} \text{h}^{-1}$) and pseudo-first-order kinetics rate constants (k).

those of NPCN. First, E_{CBM} and E_{VBM} of MPCN are considered similar to those of NPCN because E_{CBM} and E_{VBM} of MCN-x are similar to those of CN. Secondly, the E_F of MCN-2 should be the unified Fermi level of NPCN and MPCN. Then, E_F of MPCN should be higher than that of MCN-2 because the E_F of MCN-2 is higher than that of NPCN (or CN). That is, distance between E_{CBM} and E_F for MPCN is smaller than that for NPCN. Based on these, the energy band levels of NPCN/MPCN homojunctions in equilibrium are shown in Fig. 7d. An electric field was built at the interface between MPCN and NPCN when the unified E_F was formed. This electric field can accelerate photogenerated electron transfer from CB of NPCN to that of MPCN and hole transfer from VB of MPCN to that of NPCN under visible light irradiation, which significantly increases the charge separation efficiency.

3.5. Photocatalytic application

In view of above prominent difference in the charge separation efficiency, photocatalytic hydrogen evolution (PHE) rates of different samples were investigated with photodeposited Pt as a cocatalyst and active center for hydrogen evolution. As shown in Fig. 8a, MCN-x exhibits higher PHE rates ($235\text{--}934 \mu\text{mol g}^{-1} \text{h}^{-1}$) than CN ($163 \mu\text{mol g}^{-1} \text{h}^{-1}$). Their PHE rates increase then decrease with increasing x . MCN-2 exhibits the highest value which is ~5.7 times that of CN, and is comparable to most of other similar CN-based photocatalysts synthesized using MA (Table S3, Supporting Information). The apparent quantum yield of MCN-2 can reach ~9.1% at 420 nm (Fig. S14, Supporting Information), but is still lower than some reported results (Table S4, Supporting Information). The S_{BET} -normalized PHE rate of MCN-2 ($64.0 \mu\text{mol m}^{-2} \text{h}^{-1}$) is still greater than that of CN ($24.3 \mu\text{mol m}^{-2} \text{h}^{-1}$), indicating both the increased S_{BET} and accelerated charge

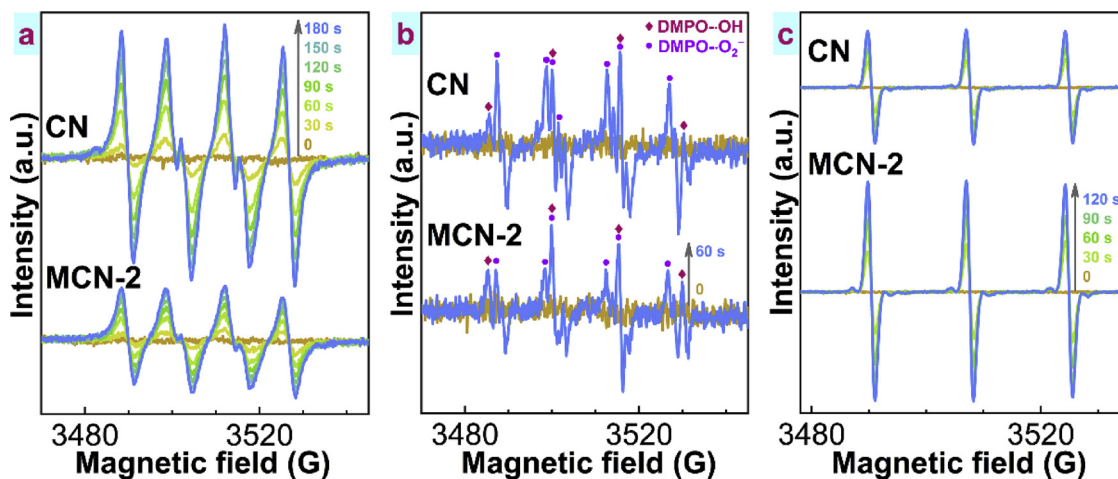


Fig. 9. EPR spectra of (a) DMPO-·O₂⁻ and (b) DMPO-·OH adducts and (c) TEMP-trapped ¹O₂ under light irradiation for different time. Time of 0 means in the dark.

separation (Fig. 7) are responsible for the photoactivity enhancement. The PHE of samples does not slow after the five-run cyclic experiments (Fig. 15a, Supporting Information), suggesting their high stability. Without Pt as a cocatalyst, neither CN nor MCN-2 exhibit detectable activity for PHE (Fig. 8a).

Photoactivity of samples in contaminant degradation was also studied. As shown in Fig. 8b, MCN-x also exhibits higher photocatalytic efficiencies than CN, and MCN-2 is also the optimal one. The RhB photodegradation data can be well fitted to a pseudo-first-order model, $-\ln C/C_0 = kt$, where t , C_0 , C , and k are the reaction time, the initial concentration, the concentration at t , and the rate constant, respectively. The k (MCN-2), 0.609 h^{-1} is ~ 3.1 times that of k (CN), 0.197 h^{-1} . Cyclic experiments for RhB photodegradation indicate that the photoactivity of MCN-2 shows no obvious decrease after five consecutive runs (Fig. S15b) and the XRD pattern and the SEM image after the cyclic experiments (Fig. S15c and d) are similar to those before (Fig. 2e), further revealing high stability of the sample. Besides, photoactivity of MCN-HClO, MCN-CYA, and MCN-CYA-W is higher than CN, but much lower than MCN-2 (Fig. S16, Supporting Information), suggesting synergism of hierarchical structure of the precursor and CYA for formation of MCN-2 with high photoactivity.

Reactive oxygen species (ROS) play key roles in photodegradation of contaminants and thus generation rates of ROS can also reflect the photocatalytic performance. Fig. 9 shows EPR spectra of DMPO-·O₂⁻, DMPO-·OH, and TEMP-trapped ¹O₂ (TEMPO). All the spectra show no signals in the dark, suggesting no ROS were generated. Fig. 9a shows six characteristic peaks of DMPO-·O₂⁻ [46] and peaks of CN are stronger than those of MCN-2 at light irradiation time of 30–180 s, indicating slower generation of ·O₂⁻ for MCN-2. Fig. 9b shows weak DMPO-·OH signals and relatively strong DMPO-·O₂⁻ signals for both CN and MCN-2 [47] under light irradiation. Formation of DMPO-·O₂⁻ is because of too slow generation of ·OH compared with ·O₂⁻. Though weak, the DMPO-·OH signal for MCN-2 is still stronger than that for CN. EPR spectra of the samples for ¹O₂ detection show a gradually strengthening 1:1:1 triplet signal of TEMPO [48] with irradiation time and MCN-2 exhibits a higher signal intensity than CN (Fig. 9c), demonstrating faster generation of ¹O₂ for the former. Overall, the faster generated ·OH and ¹O₂ for MCN-2 are the probable functional ROS for higher activity of MCN-2 in organic photodegradation.

The ·O₂⁻ and ·OH are mainly generated via reduction of O₂ by electrons and oxidation of H₂O by holes, respectively, while ¹O₂ can be produced via oxidation of ·O₂⁻ by holes or the energy transfer from the excited state of photosensitizers to the ground state of O₂ [49]. In view of the slower generation of ·O₂⁻ and faster production of ¹O₂ for MCN-2 than those for CN (Fig. 9), it can be concluded that the O introduction in MCN-2 may suppress the ·O₂⁻ generation and

meanwhile, enhance the ¹O₂ production via the energy transfer between excited triplet excitons in MCN-2 and ground-state O₂ [50,51]. This result is exciting because ¹O₂ is considered one of the most effective and selective oxygen agents [52].

4. Conclusions

CN homojunctions (MCN-x) with massive mesopores were synthesized via calcination of CYA-loaded MA hierarchical structure. The MA hierarchical structure was simply prepared for the first time in the HClO ethanol solution. The MA hierarchical structure and CYA concurrently function for formation of new massive mesopores in MCN-x. SEM and TEM images of MCN-2 show distinctly regions with new massive mesopores (MPCN) and those with few mesopores (NPCN). The new mesopore size is $\sim 2\text{--}6\text{ nm}$. Formation of these new mesopores leads to a prominent increase in S_{BET} of MCN-2. The presence of CYA or HClO in the precursor leads to oxygen introduction in the new mesopore areas of MCN-2, which causes slight enhancement in visible light absorption. The O doping and mesopore structure of MCN-2 make its energy band levels different from those of CN, i.e. the energy band levels of MPCN different from those of NPCN, which is the root cause for MPCN/NPCN homojunction fabrication. The construction of homojunction considerably accelerates the charge separation. The highest S_{BET} , accelerated charge separation, and enhanced photoabsorption of MCN-2 lead to its significant photoactivity improvement in PHE and organic degradation. Besides, the O doping can accelerate the singlet oxygen generation via the energy transfer process. This work provides a new way to prepare MA hierarchical structure and illustrates in detail the mechanism for CN homojunction construction with new mesopore generation, which can direct synthesis of similar CN-based photocatalysts.

Acknowledgements

This work was supported by the National Natural Science Foundation of China (No. 21603118 and 21573133), the Young Scholars Program of Shandong University in China (No. 2018WLJH39), and the Independent Innovation Foundation of Shandong University in China (No. 2016JC032).

Appendix A. Supplementary data

Supplementary material related to this article can be found, in the online version, at doi:<https://doi.org/10.1016/j.apcatb.2019.04.084>.

References

- [1] M.Z. Rahman, K. Davey, C.B. Mullins, Tuning the intrinsic properties of carbon nitride for high quantum yield photocatalytic hydrogen production, *Adv. Sci. 5* (2018) 1800820.
- [2] J. Fu, J. Yu, C. Jiang, B. Cheng, g-C₃N₄-based heterostructured photocatalysts, *Adv. Energy Mater. 8* (2018) 1701503.
- [3] L. Jiang, X. Yuan, G. Zeng, J. Liang, Z. Wu, H. Wang, Construction of an all-solid-state Z-scheme photocatalyst based on graphite carbon nitride and its enhancement to catalytic activity, *Environ. Sci. Nano 5* (2018) 599–615.
- [4] C. Ling, X. Niu, Q. Li, A. Du, J. Wang, Metal-free single atom catalyst for N₂ fixation driven by visible light, *J. Am. Chem. Soc. 140* (2018) 14161–14168.
- [5] Y. Zhang, L. Wu, X. Zhao, Y. Zhao, H. Tan, X. Zhao, Y. Ma, Z. Zhao, S. Song, Y. Wang, Y. Li, Leaf-mosaic-inspired vine-like graphitic carbon nitride showing high light absorption and efficient photocatalytic hydrogen evolution, *Adv. Energy Mater. 8* (2018) 1801139.
- [6] Y. Wang, F. Silveri, M.K. Bayazit, Q. Ruan, Y. Li, J. Xie, C.R.A. Catlow, J. Tang, Bandgap engineering of organic semiconductors for highly efficient photocatalytic water splitting, *Adv. Energy Mater. 8* (2018) 1801084.
- [7] P. Yang, H. Ou, Y. Fang, X. Wang, A facile steam reforming strategy to delaminate layered carbon nitride semiconductors for photoredox catalysis, *Angew. Chem. Int. Ed. 56* (2017) 3992–3996.
- [8] H. Wang, X. Sun, D. Li, X. Zhang, S. Chen, W. Shao, Y. Tian, Y. Xie, Boosting hot-electron generation: exciton dissociation at the order-disorder interfaces in polymeric photocatalysts, *J. Am. Chem. Soc. 139* (2017) 2468–2473.
- [9] Y. Yu, W. Yan, X. Wang, P. Li, W. Gao, H. Zou, S. Wu, K. Ding, Surface engineering for extremely enhanced charge separation and photocatalytic hydrogen evolution on g-C₃N₄, *Adv. Mater. 30* (2018) 1705060.
- [10] W. Lei, Y. Mi, R. Feng, P. Liu, S. Hu, J. Yu, X. Liu, J.A. Rodriguez, J.-o. Wang, L. Zheng, Hybrid 0D-2D black phosphorus quantum dots-graphitic carbon nitride nanosheets for efficient hydrogen evolution, *Nano Energy 50* (2018) 552–561.
- [11] S.A. Ansari, M.H. Cho, Growth of three-dimensional-like SnS₂ on g-C₃N₄ sheets as an efficient visible-light photocatalyst, photoelectrode, and electrochemical supercapacitance material, *Sustain. Energy Fuels 1* (2017) 510–519.
- [12] S.P. Adhikari, Z.D. Hood, Vincent W. Chen, K.L. More, K. Senevirathne, A. Lachgar, Visible-light-active g-C₃N₄/N-doped Sr₂Nb₂O₇ heterojunctions as photocatalysts for the hydrogen evolution reaction, *Sustain. Energy Fuels 2* (2018) 2507–2515.
- [13] J. Zhang, M. Zhang, R.Q. Sun, X. Wang, A facile band alignment of polymeric carbon nitride semiconductors to construct isotype heterojunctions, *Angew. Chem. Int. Ed. 51* (2012) 10145–10149.
- [14] H. Li, Y. Liu, X. Gao, C. Fu, X. Wang, Facile synthesis and enhanced visible-light photocatalysis of graphitic carbon nitride composite semiconductors, *ChemSusChem 8* (2015) 1189–1196.
- [15] V.Wh. Lau, V.Wz. Yu, F. Ehrat, T. Botari, I. Moudrakovski, T. Simon, V. Duppel, E. Medina, J.K. Stolarczyk, J. Feldmann, V. Blum, B.V. Lotsch, Urea-modified carbon nitrides: enhancing photocatalytic hydrogen evolution by rational defect engineering, *Adv. Energy Mater. 7* (2017) 1602251.
- [16] M.Z. Rahman, P.C. Tapping, T.W. Kee, R. Smernik, N. Spooner, J. Moffatt, Y. Tang, K. Davey, S.Z. Qiao, A benchmark quantum yield for water photoreduction on amorphous carbon nitride, *Adv. Funct. Mater. 27* (2017) 1702384.
- [17] C. Qiu, Y. Xu, X. Fan, D. Xu, R. Tandiana, X. Ling, Y. Jiang, C. Liu, L. Yu, W. Chen, Highly crystalline K-intercalated polymeric carbon nitride for visible-light photocatalytic alkenes and alkynes deuterations, *Adv. Sci. (2018) 1801403*.
- [18] W.J. Ong, L.L. Tan, Y.H. Ng, S.T. Yong, S.P. Chai, Graphitic carbon nitride (g-C₃N₄)-based photocatalysts for artificial photosynthesis and environmental remediation: are we a step closer to achieving sustainability? *Chem. Rev. 116* (2016) 7159–7329.
- [19] G. Liu, G. Zhao, W. Zhou, Y. Liu, H. Pang, H. Zhang, D. Hao, X. Meng, P. Li, T. Kako, J. Ye, In situ bond modulation of graphitic carbon nitride to construct p-n homojunctions for enhanced photocatalytic hydrogen production, *Adv. Funct. Mater. 26* (2016) 6822–6829.
- [20] S. Tan, Z. Xing, J. Zhang, Z. Li, X. Wu, J. Cui, J. Kuang, J. Yin, W. Zhou, Meso-g-C₃N₄/g-C₃N₄ nanosheets laminated homojunctions as efficient visible-light-driven photocatalysts, *Int. J. Hydrogen Energy 42* (2017) 25969–25979.
- [21] C. Liu, X. Dong, Y. Hao, X. Wang, H. Ma, X. Zhang, A novel supramolecular pre-organization route for improving g-C₃N₄/g-C₃N₄ metal-free homojunction photocatalysis, *New J. Chem. 41* (2017) 11872–11880.
- [22] S. Martha, S. Mansingh, K.M. Parida, A. Thirumurugan, Exfoliated metal free homojunction photocatalyst prepared by a biomediated route for enhanced hydrogen evolution and Rhodamine B degradation, *Mater. Chem. Front. 1* (2017) 1641–1653.
- [23] Z. Liu, G. Wang, H.S. Chen, P. Yang, An amorphous/crystalline g-C₃N₄ homojunction for visible light photocatalysis reactions with superior activity, *Chem. Commun. 54* (2018) 4720–4723.
- [24] Q. Liang, Z. Li, X. Yu, Z.-H. Huang, F. Kang, Q.-H. Yang, Macroscopic 3D porous graphitic carbon nitride monolith for enhanced photocatalytic hydrogen evolution, *Adv. Mater. 27* (2015) 4634–4639.
- [25] J. Zhang, M. Zhang, C. Yang, X. Wang, Nanospherical carbon nitride frameworks with sharp edges accelerating charge collection and separation at a soft photocatalytic interface, *Adv. Mater. 26* (2014) 4121–4126.
- [26] H. Li, Q. Deng, J. Liu, W. Hou, N. Du, R. Zhang, X. Tao, Synthesis, characterization and enhanced visible light photocatalytic activity of Bi₂MoO₆/Zn-Al layered double hydroxide hierarchical heterostructures, *Catal. Sci. Technol. 4* (2014) 1028–1037.
- [27] C.A. Gomes, L.M. Lube, C. Fernandes, R.W.A. Franco, J.A.L.C. Resende, A. Horn, A new system for cyclohexane functionalization employing iron(III) catalysts and trichloroisocyanuric acid, *New J. Chem. 41* (2017) 11498–11502.
- [28] Y.S. Jun, E.Z. Lee, X. Wang, W.H. Hong, G.D. Stucky, A. Thomas, From melamine-cyanuric acid supramolecular aggregates to carbon nitride hollow spheres, *Adv. Funct. Mater. 23* (2013) 3661–3667.
- [29] W. Xing, W. Tu, Z. Han, Y. Hu, Q. Meng, G. Chen, Template-induced high-crystalline g-C₃N₄ nanosheets for enhanced photocatalytic H₂ evolution, *ACS Energy Lett. 3* (2018) 514–519.
- [30] Y. Zheng, Z. Yu, H. Ou, A.M. Asiri, Y. Chen, X. Wang, Black phosphorus and polymeric carbon nitride heterostructure for photoinduced molecular oxygen activation, *Adv. Funct. Mater. 28* (2018) 1705407.
- [31] Y. Zheng, L. Lin, X. Ye, F. Guo, X. Wang, Helical graphitic carbon nitrides with photocatalytic and optical activities, *Angew. Chem. Int. Ed. 53* (2014) 11926–11930.
- [32] Y. Kang, Y. Yang, L.-C. Yin, X. Kang, G. Liu, H.-M. Cheng, An amorphous carbon nitride photocatalyst with greatly extended visible-light-responsive range for photocatalytic hydrogen generation, *Adv. Mater. 27* (2015) 4572–4577.
- [33] Z. Huang, F. Li, B. Chen, G. Yuan, Cycloaddition of CO₂ and epoxide catalyzed by amino- and hydroxyl-rich graphitic carbon nitride, *Catal. Sci. Technol. 6* (2016) 2942–2948.
- [34] S. Martha, A. Nashim, K.M. Parida, Facile synthesis of highly active g-C₃N₄ for efficient hydrogen production under visible light, *J. Mater. Chem. A 1* (2013) 7816–7824.
- [35] G. Tian, Y. Chen, W. Zhou, K. Pan, Y. Dong, C. Tian, H. Fu, Facile solvothermal synthesis of hierarchical flower-like Bi₂MoO₆ hollow spheres as high performance visible-light driven photocatalysts, *J. Mater. Chem. 21* (2011) 887–892.
- [36] T.L. Barr, S. Seal, Nature of the use of adventitious carbon as a binding energy standard, *J. Vac. Sci. Technol. A 13* (1995) 1239–1246.
- [37] S. Yu, J. Li, Y. Zhang, M. Li, F. Dong, T. Zhang, H. Huang, Local spatial charge separation and proton activation induced by surface hydroxylation promoting photocatalytic hydrogen evolution of polymeric carbon nitride, *Nano Energy 50* (2018) 383–392.
- [38] P. Niu, M. Qiao, Y. Li, L. Huang, T. Zhai, Distinctive defects engineering in graphitic carbon nitride for greatly extended visible light photocatalytic hydrogen evolution, *Nano Energy 44* (2018) 73–81.
- [39] G. Zhang, M. Zhang, X. Ye, X. Qiu, S. Lin, X. Wang, Iodine modified carbon nitride semiconductors as visible light photocatalysts for hydrogen evolution, *Adv. Mater. 26* (2014) 805–809.
- [40] F.-Y. Su, C.-Q. Xu, Y.-X. Yu, W.-D. Zhang, Carbon self-doping induced activation of n-π* electronic transitions of g-C₃N₄ nanosheets for efficient photocatalytic H₂ evolution, *ChemCatChem 8* (2016) 3527–3535.
- [41] P. Qiu, C. Xu, H. Chen, F. Jiang, X. Wang, R. Lu, X. Zhang, One step synthesis of oxygen doped porous graphitic carbon nitride with remarkable improvement of photo-oxidation activity: role of oxygen on visible light photocatalytic activity, *Appl. Catal. B 206* (2017) 319–327.
- [42] M. Ran, J. Li, W. Cui, Y. Li, P. Li, F. Dong, Efficient and stable photocatalytic NO removal on C self-doped g-C₃N₄: electronic structure and reaction mechanism, *Catal. Sci. Technol. 8* (2018) 3387–3394.
- [43] N. Meng, J. Ren, Y. Liu, Y. Huang, T. Petit, B. Zhang, Engineering oxygen-containing and amino groups into two-dimensional atomically-thin porous polymeric carbon nitrogen for enhanced photocatalytic hydrogen production, *Energy Environ. Sci. 11* (2018) 566–571.
- [44] L. Li, J. Yan, T. Wang, Z.-J. Zhao, J. Zhang, J. Gong, N. Guan, Sub-10 nm rutile titanium dioxide nanoparticles for efficient visible-light-driven photocatalytic hydrogen production, *Nat. Commun. 6* (2015) 5881.
- [45] G. Zhang, Z.-A. Lan, L. Lin, S. Lin, X. Wang, Overall water splitting by Pt/g-C₃N₄ photocatalysts without using sacrificial agents, *Chem. Sci. 7* (2016) 3062–3066.
- [46] Y. Zhu, Z. Chen, T. Gao, Q. Huang, F. Niu, L. Qin, P. Tang, Y. Huang, Z. Sha, Y. Wang, Construction of hybrid Z-scheme Pt/CdS-TNTAs with enhanced visible-light photocatalytic performance, *Appl. Catal. B 163* (2015) 16–22.
- [47] S. Pou, W.S. Pou, D.S. Bredt, S.H. Snyder, G.M. Rosen, Generation of superoxide by purified brain nitric oxide synthase, *J. Biol. Chem. 267* (1992) 24173–24176.
- [48] S. Wang, X. Ding, X. Zhang, H. Pang, X. Hai, G. Zhan, W. Zhou, H. Song, L. Zhang, H. Chen, J. Ye, In Situ carbon homogeneous doping on ultrathin bismuth molybdate: a dual-purpose strategy for efficient molecular oxygen activation, *Adv. Funct. Mater. 27* (2017) 1703923.
- [49] Y. Nosaka, A.Y. Nosaka, Generation and detection of reactive oxygen species in photocatalysis, *Chem. Rev. 117* (2017) 11302–11336.
- [50] H. Wang, S. Jiang, S. Chen, X. Zhang, W. Shao, X. Sun, Z. Zhao, Q. Zhang, Y. Luo, Y. Xie, Insights into the excitonic processes in polymeric photocatalysts, *Chem. Sci. 8* (2017) 4087–4092.
- [51] H. Wang, S. Jiang, S. Chen, D. Li, X. Zhang, W. Shao, X. Sun, J. Xie, Z. Zhao, Q. Zhang, Y. Tian, Y. Xie, Enhanced singlet oxygen generation in oxidized graphitic carbon nitride for organic synthesis, *Adv. Mater. 28* (2016) 6940–6945.
- [52] W. Wu, Q. Zhang, X. Wang, C. Han, X. Shao, Y. Wang, J. Liu, Z. Li, X. Lu, M. Wu, Enhancing selective photooxidation through Co-Nx-doped carbon materials as singlet oxygen photosensitizers, *ACS Catal. 7* (2017) 7267–7273.